Bioorganic Chemistry 103 (2020) 104145

Contents lists available at ScienceDirect

Bioorganic Chemistry

journal homepage: www.elsevier.com/locate/bioorg

Hydroxynaphthalenecarboxamides and substituted piperazinylpropandiols, two new series of BRAF inhibitors. A theoretical and experimental study

Ludmila E. Campos[a], Francisco Garibotto[a], Emilio Angelina[b], Jiri Kos[c], Tomas Gonec[d], Pavlina Marvanova[d], Marcela Vettorazzi[a], Michal Oravec[e], Izabela Jendrzejewska[f], Josef Jampilek[c], Sergio E. Alvarez[a,*], Ricardo D. Enriz[a,*]

[a] Facultad de Química, Bioquímica y Farmacia, Universidad Nacional de San Luis, Instituto Multidisciplinario de Investigaciones Biológicas (IMIBIO-SL), Ejército de los Andes 950, 5700 San Luis, Argentina
[b] Laboratorio de Estructura Molecular y Propiedades, Área de Química Física, Departamento de Química, Facultad de Ciencias Exactas y Naturales y Agrimensura, Universidad Nacional del Nordeste, Avda. Libertad 5460, (3400) Corrientes, Argentina
[c] Regional Centre of Advanced Technologies and Materials, Faculty of Science, Palacky University, Slechtitelu 27, 78371 Olomouc, Czech Republic
[d] Department of Chemical Drugs, Faculty of Pharmacy, Masaryk University, Palackeho 1, 612 00 Brno, Czech Republic
[e] Global Change Research Institute CAS, Belidla 986/4a, 603 00 Brno, Czech Republic
[f] Institute of Chemistry, University of Silesia, Szkolna 9, 40007 Katowice, Poland

ARTICLE INFO

Keywords:
BRAF inhibitors
Melanoma
Molecular modeling
Cell viability
ERK phosphorylation

ABSTRACT

The oncogenic mutated kinase $BRAF^{V600E}$ is an attractive molecular target because it is expressed in several human cancers, including melanoma. To present, only three BRAF small inhibitors are approved by the FDA for the treatment of patients with metastatic melanoma: Vemurafenib, Dabrafenib and Encorafenib. Although many protocol treatments have been probed in clinical trials, BRAF inhibition has a limited effectiveness because patients invariably develop resistance and secondary toxic effects associated with the therapy. These limitations highlight the importance of designing new and better inhibitors with different structures that could establish different interactions in the active site of the enzyme and therefore decrease resistance progress.

Considering the data from our previous report, here we studied two series of derivatives of structural scaffolds as potential BRAF inhibitors: hydroxynaphthalenecarboxamides and substituted piperazinylpropandiols. Our results indicate that structural analogues of substituted piperazinylpropandiols do not show significantly better activities to that previously reported. In contrast, the hydroxynaphthalenecarboxamides derivatives significantly inhibited cell viability and ERK phosphorylation, a measure of BRAF activity, in Lu1205 $BRAF^{V600E}$ melanoma cells. In order to better understand these experimental results, we carried out a molecular modeling study using different combined techniques: docking, MD simulations and quantum theory of atoms in molecules (QTAIM) calculations. Thus, by using this approach we determined that the molecular interactions that stabilize the different molecular complexes are closely related to Vemurafenib, a well-documented BRAF inhibitor. Furthermore, we found that bi-substituted compounds may interact more strongly respect to the mono-substituted analogues, by establishing additional interactions with the DFG-loop at the BRAF-active site. On the bases of these results we synthesized and tested a new series of hydroxynaphthalenecarboxamides bi-substituted. Remarkably, all these compounds displayed significant inhibitory effects on the bioassays performed. Thus, the structural information reported here is important for the design of new $BRAF^{V600E}$ inhibitors possessing this type of structural scaffold.

1. Introduction

After the publication in 2002 of the first article describing an oncogenic BRAF mutant protein [1,2], intense efforts have been centered in the development of selective and potent BRAF inhibitors. Certainly, US Food and Drug Administration (FDA) support the use of two $BRAF^{V600E}$ inhibitors for the treatment of metastatic melanoma: Vemurafenib (Zelboraf) and Dabrafenib (Tafinlar), approved in 2011 and 2013, respectively [3,4]. Although both drugs showed an impressive success rate in melanoma patients, durability of response remains an issue because the tumor quickly becomes resistant [5]. On the other hand, many cancers are intrinsically resistant to these compounds or

* Corresponding authors.
E-mail addresses: sealvarez98@gmail.com (S.E. Alvarez), denriz@unsl.edu.ar (R.D. Enriz).

https://doi.org/10.1016/j.bioorg.2020.104145
Received 16 April 2020; Received in revised form 17 June 2020; Accepted 24 July 2020
Available online 28 July 2020

show limited benefits. For example, it has been shown that colorectal and thyroid $BRAF^{V600E}$ tumors are resistant to Vemurafenib and Dabrafenib [6,7]. Recently, on the basis of COLUMBUS trial, FDA has approved a new BRAF inhibitor named Encorafenib (Array Biopharma) administrated with a MEK inhibitor for the treatment of metastatic melanoma [8,9].

In the past few years, a large number of new BRAF inhibitors have been developed [10]. Intense investigations on the biochemical and cellular effects of these new BRAF inhibitors have enlarged our understanding on their mechanisms of action [11]. It has been widely reported that BRAF inhibitors induce allosteric structural rearrangements, locking their target kinases in discrete conformations and resemble inactive or active kinase states of the αC-helix and DFG motif [12,13]. Such conformations allow to classify inhibitors as type I (αC-helix-IN/DFG-IN), type II (αC-helix-IN/DFG-OUT), or type I1/2 (αC-helix-OUT/DFG-IN) [14,15]. Both Vemurafenib and Dabrafenib belong to type I1/2 inhibitors. A recent work from Agianian and Gavathiotis show the different zones in which BRAF inhibitors would be linked [16]. Moreover, a large number of structures have been classified as first, second and third generation BRAF inhibitors.

Although BRAF is an excellent molecular target for searching new anticancer agents, its anomalous or unusual behavior implies a severe drawback for the development of new inhibitors [17–19]. While the inhibitors suppressed tumors harboring $BRAF^{V600E}$ or other BRAF mutants, they paradoxically activate RAF activity and downstream ERK signaling (RAF inhibitor paradox or "paradoxical activation") in tumors expressing BRAF wild type ($BRAF^{WT}$) [20,21]. The general consensus is that type I inhibitors exhibit more paradoxical activation, followed by type II and type I1/2. The model of "paradoxical activation" described above explains the clinical effectiveness of the current FDA approved αC-OUT RAF inhibitors Vemurafenib and Dabrafenib [22]. Moreover, paradox breakers constitute a new class of BRAF inhibitors that could inhibit $BRAF^{V600E}$ but not promotes paradoxical activation of MAPK signaling [23]. Encorafenib is the latest BRAF inhibitor FDA-approved, and in fact has shown significantly less paradoxical effects compared to Vemurafenib and Dabrafenib in patients treated with these drugs [24]. These evidences point that the rational design of new BRAF inhibitors with different structural scaffolds may establish distinct interactions with the enzyme and hence reduce resistance and paradoxical effects in order to achieve a durable response.

It is clearly evident that new BRAF inhibitors with different structural scaffolds that can bind to the enzyme in a different manner are needed. Certainly, we have recently reported a study conducted through a virtual screening in which we found three different structural scaffolds with significant inhibitory activities on BRAF [25]. These series are: 1*H*-pyrrol-2-ylcarbonylamino-1,3-benzothiazol-2-ylaminooxo carboxylic acids (Fig. 1, compounds type A), substituted piperazinylpropandiols (Fig. 1, compounds Type B) and hydroxynaphthalenecarboxamides (Fig. 1, compounds type C). From these three series of compounds, molecules **3** and **22** shown in Fig. 1 exhibited the most significant inhibitory effect. Here, we report a deeper study on two of these series by using several analogues of compounds **3** and **22**. Using molecular modeling studies we established a structure–activity relationship in these series of compounds. In addition, to gain a better understanding of the mechanisms of action at molecular level, we have carried out an exhaustive study about molecular interactions that stabilize the different ligand-receptor (L-R) complexes. Such information is of great value to perform future structural changes in these compounds that could potentially improve their affinity with the enzyme.

2. Experimental section

2.1. Chemistry

All reagents were purchased from Merck (Sigma-Aldrich, St. Louis, MO, USA) and Alfa (Alfa-Aesar, Ward Hill, MA, USA). Reactions were performed using a CEM Discover SP microwave reactor (CEM, Matthews, NC, USA). TLC experiments were performed on alumina-backed silica gel 40 F254 plates (Merck, Darmstadt, Germany). The plates were illuminated under UV (254 nm) and evaluated in iodine vapour. Melting points were determined on a Koflerhot-plate apparatus (HMK Franz KustnerNacht BG, Dresden, Germany) and are uncorrected. Infrared (IR) spectra were recorded on a Smart MIRacle ATR ZnSe for Nicolet Impact 410 FT-IR spectrometer (Thermo Scientific, West Palm Beach, FL, USA). The spectra were obtained by the accumulation of 64 scans with 2 cm^{-1} resolution in the region of 4000–650 cm^{-1}. All ^{1}H- and ^{13}C NMR spectra were recorded on a JEOL JNM-ECA 600II NMR spectrometer (600 MHz for ^{1}H and 150 MHz for ^{13}C, Jeol, Tokyo, Japan) in dimethyl sulfoxide-d_6 (DMSO-d_6), ^{1}H and ^{13}C chemical shifts (δ) are reported in ppm. Mass spectra were measured using a LTQ Orbitrap Hybrid Mass Spectrometer (Thermo Electron Corporation) with direct injection into an APCI source (400 °C) in the positive or negative mode.

1-(3-{4-[(Butoxycarbonyl)amino]benzoyloxy}-2-hydroxypropyl)-4-phenylpiperazin-1-ium chloride (3) was described by Vettorazzi*et al* [26]. 1-{2-Hydroxy-3-[(4-alkoxybenzoyl)oxy]propyl}-4-arylpiperazinediium dichlorides compounds **4–7** were published by Marvanova*et al* [27]and 1-(2-hydroxy-3-{[4-(2-propoxyethoxy)benzoyl]oxy}propyl)-4-phenylpiperazinediium dichloride (compound **8**) was published by Marvanova*et al* [28]. Described anilides**9–11** [29], **12** [30], **15–17** [31], **18** and**19** [32], and **20–25** [33]were characterized recently.

General procedures for synthesis of *N*-(substituted phenyl)naphthalene-carboxamides. The appropriate naphthalenecarboxylic acid (5.3 mM) was suspended in dry chlorobenzene (30 mL) at ambient temperature and phosphorus trichloride (2.7 mM, 0.5 eq.), and the corresponding substituted aniline (5.3 mM, 1 eq.) was added dropwise. The reaction mixture was transferred to the microwave reactor at 130 °C for 40 min, where the synthesis was performed. Then the mixture was cooled to 40 °C, and then the solvent was removed to dryness under reduced pressure. The residue was washed with 2 M HCl. The crude product was recrystallized from EtOH.

***N*-(3,5-Dichlorophenyl)-2-hydroxynaphthalene-1-carboxamide (13)**. Yield 67%; mp 246–249 °C; IR (cm^{-1}): 3362, 1646, 1586, 1538, 1514, 1448, 1436, 1403, 1352, 1312, 1299, 1262, 1231, 1211, 1114, 966, 838, 806, 795, 745, 665; ^{1}H NMR (DMSO-d_6), δ: 10.77 (s, 1H), 10.26 (s, 1H), 7.90 (d, 2H, J = 4.4 Hz), 7.86 (d, 2H, J = 7.7 Hz), 7.67 (d, 1H, J = 8.4 Hz), 7.48 (td, 1H, J = 7.8, J = 1.1 Hz), 7.34 (td, 1H, J = 7.5 Hz, J = 1.1 Hz), 7.33 (s, 1H), 7.26 (d, 1H, J = 8.8 Hz); ^{13}C NMR (DMSO-d_6), δ: 166.42, 151.87, 141.81, 134.14, 131.18, 130.66, 128.04, 127.34, 127.23, 123.19, 123.17, 122.54, 118.28, 117.70, 117.32; HR-MS: for $C_{17}H_{10}NO_2Cl_2[M\text{-}H]^+$ calculated 330.00831 *m/z*, found 330.00946 *m/z*.

2-Hydroxy-N-(3,4,5-trichlorophenyl)naphthalene-1-carboxamide(14). Yield 69%; mp 182–186 °C; IR (cm^{-1}): 3359, 3275, 1646, 1625, 1579, 1567,1511, 1505, 1434, 1382, 1372, 1302, 1273, 1235, 1189, 1151, 966, 855, 810, 787, 749, 699, 867, 657; ^{1}H NMR (DMSO-d_6), δ: 10.82 (s, 1H), 10.27 (br. s, 1H), 8.08 (s, 2H), 7.88 (t, 2H, J = 9.2 Hz), 7.67 (d, 1H, J = 8.4 Hz), 7.47 (ddd, 1H, J = 8.5 Hz, J = 6.8 Hz, J = 1.3 Hz), 7.31–7.38 (m, 1H), 7.26 (d, 1H, J = 9.0 Hz); ^{13}C NMR (DMSO-d_6), δ: 166.49, 151.93, 139.50, 132.90, 131.14, 130.78, 128.04, 127.32, 127.26, 123.35, 123.19, 123.16, 119.18, 118.26, 117.48; HR-MS: for $C_{17}H_9NO_2Cl_3$ $[M-H]^+$ calculated 363.96934 *m/z*, found 363.97052 *m/z*.

***N*-[2,4-bis(Trifluoromethyl)phenyl]-6-hydroxynaphthalene-2-carboxamide (26)**. Yield 42%; mp167-169 °C; IR (cm^{-1}): 3304, 1654, 1628, 1529, 1343, 1314, 1279, 1253, 1182, 1166, 1118, 1080, 1056, 914, 861, 841, 803, 764, 742, 675, 654; ^{1}H NMR (DMSO-d_6), δ: 10.38 (s, 1H), 10.15 (br.s, 1H), 8.48 (s, 1H), 8.15 (d, J = 8.9 Hz, 1H), 8.13 (s, 1H), 7.94 (d, J = 8.9 Hz, 1H), 7.92 (dd, J = 8.6 Hz, J = 1.7 Hz, 1H), 7.89 (d, J = 8.2 Hz, 1H), 7.83 (d, J = 8.2 Hz, 1H), 7.22 (d, J = 2.1 Hz,

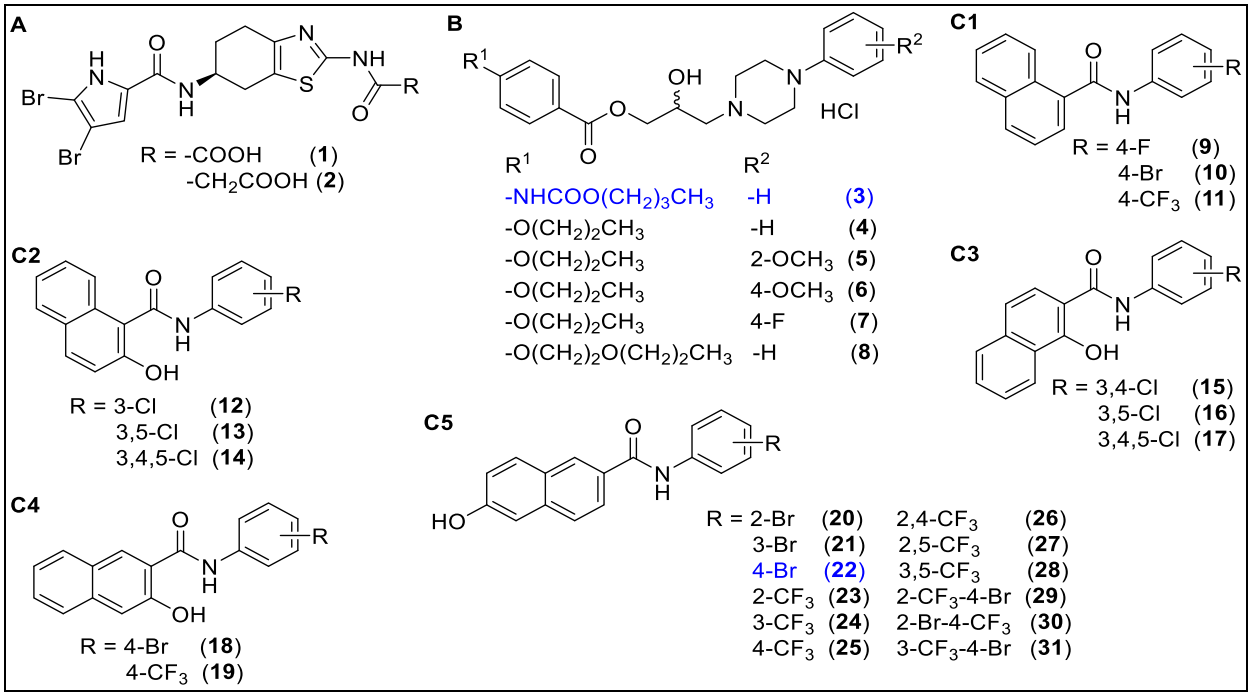

Fig. 1. Structures of investigated compounds.

1H), 7.20 (dd, J = 8.9 Hz, J = 2.1 Hz, 1H); ^{13}C NMR (DMSO-d_6), δ: 166.56, 157.34, 140.14, 136.53, 131.99, 130.88, 130.13 (q, J = 2.9 Hz), 128.46, 127.47, 127.44 (q, J = 33.2 Hz), 126,67 (q, J = 30.3 Hz), 126.56, 126.30, 124.47, 123.99–123.87 (m, 1C), 123.40 (q, J = 271.7), 122.89 (q, J = 273.1), 119.70, 108.72; HR-MS: for $C_{19}H_{10}NO_2F_6$ [M−H]$^-$ calculated 398.06212 *m/z*, found 398.06271 *m/z*.

***N*-[2,5-bis(Trifluoromethyl)phenyl]-6-hydroxynaphthalene-2-carboxamide (27)**. Yield 49%; mp179-180 °C; IR (cm^{-1}): 3361, 1609, 1591, 1534, 1494, 1433, 1393, 1336, 1313, 1284, 1260, 1181, 1121, 1085, 1042, 935, 870, 861, 835, 750; ^{1}H NMR (DMSO-d_6), δ: 10.38 (s, 1H), 10.14 (s, 1H), 8.48 (s, 1H), 8.07 (d, J = 8.2 Hz, 1H), 8.03 (s, 1H), 7.94–7.92 (m, 3H), 7.82 (d, 1H), 7.22–7.19 (m, 2H); ^{13}C NMR (DMSO-d_6), δ: 168.71, 157.30, 137.30, 136.51, 133.18 (q, J = 33.2 Hz), 130.86, 129.89 (q, J = 30.3 Hz), 128.42, 128.26 (q, J = 4.3 Hz), 127.93–127.85 (m, 1C), 127.52, 128.55, 126.25, 124.51, 124.13–124.05 (m, 1C), 123.18 (q, J = 273.1 Hz), 122.94 (q, J = 274.6 Hz), 119.68, 108.72; HR-MS: for $C_{19}H_{10}NO_2F_6$ [M−H]$^-$ calculated 398.06212 *m/z*, found 398.06243 *m/z*.

***N*-[3,5-bis(Trifluoromethyl)phenyl]-6-hydroxynaphthalene-2-carboxamide (28)**. Yield 46%; mp214-215 °C; IR (cm^{-1}): 3325, 3124, 1628, 1561, 1473, 1427, 1374, 1273, 1200, 1166, 1129, 950, 932, 885, 841, 824, 809, 697, 682, 662; ^{1}H NMR (DMSO-d_6), δ: 10.88 (s, 1H), 10.17 (s, 1H), 8.57 (s, 2H), 8.53 (d, J = 0.9 Hz, 1H), 7.96–7.94 (m, 2H), 7.83 (d, J = 8.7 Hz, 1H), 7.80 (s, 1H), 7.22–7.19 (m, 2H); ^{13}C NMR (DMSO-d_6), δ: 166.34, 157.47, 141.37, 136.60, 130.89, 130.65 (q, J = 33.2 Hz), 128.49, 127.82, 126.49, 126.34, 124.50, 123.34 (q, J = 273.1 Hz), 119.80–119.70 (m, 2C), 116.20–116.06 (m, 1C), 108.77; HR-MS: for $C_{19}H_{10}NO_2F_6$ [M−H]$^-$ calculated 398.06212 *m/z*, found 398.06268 *m/z*.

***N*-[4-Bromo-2-(trifluoromethyl)phenyl]-6-hydroxynaphthalene-2-carboxamide (29)**. Yield 45%; mp209-211 °C; IR (cm^{-1}): 3260, 1613, 1577, 1519, 1502, 1475, 1435, 1407, 1394, 1355, 1297, 1286, 1266, 1200, 1164, 1115, 1049, 909, 887, 859, 819, 808, 764, 726, 681; ^{1}H NMR (DMSO-d_6), δ: 10.20 (s, 1H), 10.12 (s, 1H), 8.46 (s, 1H), 8.00 (d, J = 1.8 Hz, 1H), 7.96 (dd, J = 8.7 Hz, 2,3 Hz, 1H), 7.92 (d, J = 8.7 Hz, 1H), 7.90 (dd, J = 8.2 Hz, J = 1.4 Hz, 1H), 7.81 (d, J = 8.7 Hz, 1H), 7.55 (d, J = 8.2 Hz, 1H), 7.21–7.17 (m, 2H); ^{13}C NMR (DMSO-d_6), δ: 166.49, 157.23, 136.43, 136.09, 135.57 (q, J = 1.9 Hz), 133.35, 130.83, 129.28 (q, J = 5.8 Hz), 128.31, 127.86 (q, J = 29.9 Hz), 127.66, 126.56, 126.22, 124.47, 122.67 (q, J = 273.6 Hz), 119.64, 119.63, 108.69; HR-MS: for $C_{18}H_{10}O_2NBrF_3$ [M−H]$^-$ calculated 407.98524 *m/z*, found 407.98630 *m/z*.

***N*-[2-Bromo-4-(trifluoromethyl)phenyl]-6-hydroxynaphthalene-2-carboxamide (30)**. Yield 42%; mp184-186 °C; IR (cm^{-1}): 3263, 1662, 1680, 1579, 1521, 1486, 1471, 1436, 1393, 1317, 1263, 1195, 1165, 1117, 1076, 1041, 966, 945, 887, 879, 863, 834, 805, 742, 687; ^{1}H NMR (DMSO-d_6), δ: 10.21 (s, 1H), 10.15 (s, 1H), 8.53 (s, 1H), 8.12 (d, J = 0.9 Hz, 1H), 7.96–7.91 (m, 3H), 7.83 (d, J = 8.7 Hz, 2H), 7.22–7.18 (m, 2H); ^{13}C NMR (DMSO-d_6), δ: 165.53, 157.36, 140.75, 136.55, 130.91, 129.66 (q, J = 3.9 Hz), 128.51, 128.25, 127.62, 127.34 (q, J = 32.8 Hz), 126.57, 126.32, 125.15 (q, J = 3.9 Hz), 124.48, 123.29 (q, J = 273.6 Hz), 119.86, 119.69, 108.72; HR-MS: for $C_{18}H_{10}O_2NBrF_3$ [M−H]$^-$ calculated 407.98524 *m/z*, found 407.98571 *m/z*.

***N*-[4-Bromo-3-(trifluoromethyl)phenyl]-6-hydroxynaphthalene-2-carboxamide (31)**. Yield 60%; mp198-201 °C; IR (cm^{-1}): 3353, 3282, 1664, 1632, 1601, 1538, 1506, 1428, 1315, 1266, 1237, 12008, 1174, 1133, 1123, 1020, 908, 887, 870, 836, 802, 764, 742, 715, 672, 648; ^{1}H NMR (DMSO-d_6), δ: 10.68 (s, 1H), 10.14 (s, 1H), 8.49 (s, 1H), 8.4 (d, J = 2.7 Hz, 1H), 8.09 (dd, J = 8.7 Hz, J = 2.3 Hz, 1H), 7.94 (d, J = 8.7 Hz, 1H), 7.93 (dd, J = 8.7 Hz, J = 1.8 Hz, 1H), 7.87 (d, J = 9.1 Hz, 1H), 7.82 (d, J = 8.7 Hz, 1H), 7.21–7.18 (m, 2H); ^{13}C NMR (DMSO-d_6), δ: 166.09, 157.35, 139.40, 136.48, 135.40, 130.87, 128.44 (q, J = 30.8 Hz), 128.35, 128.16, 126.51, 126.27, 124.88, 124.55, 122.94 (q, J = 272.6 Hz), 119.69, 119.18 (q, J = 5.8 Hz), 111.65 (q, J = 1.9 Hz), 108.74; HR-MS: for $C_{18}H_{10}O_2NBrF_3$ [M−H]$^-$ calculated 407.98524 *m/z*, found 407.98549 *m/z*.

2.2. Bioassays

2.2.1. Reagents

Stock solutions of Vemurafenib and compounds tested in the present work were prepared in sterile DMSO, properly aliquoted and preserved at −20 °C. Vemurafenib was included in all the experiments as a

positive control of pERK and viability inhibition.

Anti-ERK total (dilution 1/2000) and phospho-ERK (T202-Y204, dilution 1/1000) antibodies were obtained from Cell Signaling (Danvers, MA, USA) and prepared in TBS buffer (20 mM Tris pH 7.4 and 0.9% NaCl) supplemented with 5% BSA (bovine serum albumin) and 0.1% Tween-20. Secondary antibodies conjugated to near-infrared fluorochromes (IRD, dilution 1/30.000) were from Li-COR (Lincoln, NE, USA) and prepared as indicated [25].

A stock solution of 5 mg/mL of MTT (3-(4,5-Dimethyl-2-thiazolyl)-2,5-diphenyl-2H-tetrazolium bromide, Sigma Aldrich) viability reagent was prepared freshly in PBS by five consecutive cycles of 15′ vortexing and 2′ sonication. After centrifugation at 12.000 *xg*, 4 °C for 10′, the supernatant was recovered and MTT reagent diluted 1:10 in DMEM serum free and stored at 4 °C as described previously [25].

2.2.2. Cell culture

Lu1205 $BRAF^{V600E}$ (mutant) melanoma cells were used to perform all the bioassays. Cells were cultured in Dulbecco's Modified Eagle's Media (DMEM, Gibco) supplemented with 10% of fetal bovine serum (Natocor), as described previously [25]. Cells were obtained from Dr. Pablo Bergami (Universidad de Maimónides, Buenos Aires, Argentina).

2.2.3. Western blot

Western blot experiments were performed essentially as described [25]. Briefly, 40.000 Lu1205 cells/well were seeded in 12-well plates and grown for 72 h. Medium was replaced by fresh medium containing the compound (1 and 10 μM), and cells cultured for 2 additional hours at 37 °C. Cells were washed with ice-cold PBS and scraped into lysis buffer containing 20 mM Tris-HCl (pH 7.4), 1 mM EDTA, 150 mM NaCl, 1% Triton X-100, 1 mM ß-mercaptoethanol, 1 mM Na_3VO_4, and 1:2 protease inhibitor cocktail (Roche). Lysates were incubated on ice for 1 h and centrifuged at 10.000 *xg* for 15 min to remove cellular debris. Equal amounts of proteins (30 μg) were separated by SDS-PAGE and then transblotted to nitrocellulose, blocked with 3% nonfat dry milk for 1 h at room temperature, and then incubated overnight at 4 °C with specific primary antibodies as indicated in each figure. Immunoreactive signals were detected by 1 h-incubation at room temperature with appropriate secondary antibodies (IRD, Li-COR, 1/30.000). After scanning in Oddyssey Clx device, optical densities of pERK bands were quantified and normalized to their respective total ERK bands with Image Studio 5.2 Software.

2.2.4. Cell viability assay

All the viability experiments were performed in sextuplicates for each concentration and each compound as reported [25]. In brief, 5000 Lu1205 cells/well were grown for 18 h in 96-well plates and after that, the medium was replaced by fresh medium containing the indicated compounds (final concentration 1 and 10 μM) or DMSO vehicle and cultured for another 72 h. Lu1205 cells were then incubated for 3 additional hours in 110 μl of 0.5 mg/ml solution of MTT. Formazan was solubilized with DMSO and the concentration detected by absorbance at 540 nm (Epoch). Average absorbance of each treatment (six replicates) was normalized with average absorbance of the respective control.

2.2.5. Statistics

One way-ANOVA analysis and Tukey's post-test were used to determine the significance of western blot and cell viability bioassays.

2.3. Molecular modeling

2.3.1. Docking study

The docking simulations were carried out using AutoDock 4.2 [34]. In all simulations the following parameters were used: initial population of trial ligands was constituted by 250 individuals; maximum number of generations was set to 2.7×10^4. The maximum number of energy evaluations was 10.0×10^6. All other run parameters were maintained at their default setting. The 3D affinity map was a cube which size was chosen depending on the size of the binding pocket of each system. The points were separated by 0.375 Å and centered at the active site of the different molecular targets. The resulting docked conformations were clustered into families by the backbone RMSD (root mean square deviation) of 2 Å. Considering that the docking calculations suggest several modes of binding for each compound and the binding energies between the clusters are similar, the leader of the most populated cluster was selected for further study.

2.3.2. Refinement of the anchoring

After docking calculations, the complexes were refined by performing molecular dynamics simulations. Antechamber Software in the AmberTools package [35] was used to generate the parameters for MD simulations considering ff99SB and GAFF force fields [36,37]. All MD simulations were performed with the Amber 16 software package (All-atoms force field ff99SB) using periodic boundary conditions for constant volume and cubic simulation cells [38]. Each model was soaked in a truncated octahedral periodic box of TIP3P water molecules. The distance between the edges of the water box and the closest atom of the solutes was at least 10 Å. Sodium or chloride ions (depending on the complex) were added to neutralize the charge of the system. The entire system was subjected to energy minimization. The particle mesh Ewald method (PME) [39]was applied using a grid spacing of 1.2 Å, a spline interpolation order of 4 and a real space direct sum cutoff of 10 Å. The SHAKE algorithm was applied allowing for an integration time step of 2 fs. MD simulations were carried out at 310 K temperature. Three MD simulations of 30 ns were conducted for each system under different starting velocity distribution functions; thus, in total 90 ns were simulated for each complex. The NPT ensemble was employed using Berendsen coupling to a baro/thermostat (target pressure 1 atm, relaxation time 0.1 ps). Post MD analysis was carried out with program CPPTRAJ [40].

2.3.3. Binding energy calculations

The MM-PBSA and MM-GBSA protocol was applied to each MD trajectory in order to calculate the relative binding energies of the different complexes. The MM-PBSA and MM-GBSA method was used in a hierarchical strategy, and the details of this method have been presented elsewhere [41]. This protocol was applied to 15,000 equidistant snapshots extracted from the last 25.0 ns of the dynamics in triplicate and was used within the one-trajectory approximation.

Briefly, the binding free energy (ΔG_{bind}) resulting from the formation of a L-R complex between a ligand (L) and a receptor (R) is calculated as:

$$\Delta G_{bind} = \Delta E_{MM} + \Delta G_{solv} - T\Delta S \quad (1)$$

$$\Delta E_{MM} = \Delta E_{internal} + \Delta E_{electrostatic} + \Delta E_{vdW} \quad (2)$$

$$\Delta G_{solv} = \Delta G_{PB} + \Delta G_{SA} \quad (3)$$

where ΔE_{MM}, ΔG_{solv}, and $-T\Delta S$ are the changes in the gas phase MM energy, the solvation free energy, and the conformational entropy upon binding, respectively. ΔE_{MM} includes $\Delta E_{internal}$ (bond, angle, and dihedral energies), $\Delta E_{electrostatic}$ (electrostatic), and ΔE_{vdW} (van der Waals) energies. ΔG_{solv} is the sum of electrostatic solvation energy (polar contribution), ΔG_{PB}, and the non-electrostatic solvation component (nonpolar contribution), ΔG_{SA}. Polar contribution is calculated using the PB model, while the nonpolar energy is estimated by solvent accessible surface area. The conformational entropy change $-T\Delta S$ is usually computed by normal mode analysis, but in this study the entropy contributions were not calculated due to the computational cost involved in such calculations.

2.3.4. Selection of the input structures for QTAIM analysis

It is important to keep in mind that QTAIM calculations are

performed over static geometries, while ligand-receptor binding is a consequence of an assembly of conformations. Therefore the choice on which structure or structures must be considered in the analysis is a very important decision. To solve this problem, clustering technique was carried out using the CPPTRAJ program, included in the AmberTools package. The last 25 ns of each trajectory were analyzed resulting in a total of 5,000 frames. Thus, a total of 15,000 frames were evaluated. The representative structure of the cluster most populated for each complex was employed as input structure for the QTAIM analysis.

2.3.5. Construction of reduced models employed in QTAIM analysis.

Reduced models are necessary since the inhibitors that interact in the different active sites constitute a molecular system that is too large for precise calculations of quantum mechanics. By using a reduced model, the complexities of considering the whole biological system are avoided. Therefore, a better understanding of the inherent electronic properties of the complexes can be obtained. To determine which amino acids should be included in the reduced model, two conditions were established: i) to consider all those amino acids that are within a radius of 5 Å of distance of each of the ligand atoms and ii) to have significant interactions with the ligand. Thus, only those amino acids involved in the interactions that form the different L-R complexes were included; however, we must be sure that all the important interactions have been considered. To gain more detailed information about the molecular interactions (MI) driving the linkages of the ligands into the different active sites, the structure affinity relationship was carried out by using analysis per residue from MM-GBSA calculations. All the water molecules within a 5 Å radius were also included in the reduced model. Reduced 3D model systems representing the different L-R binding pocket of the selected zone were constructed from MD simulations; such reduced model was constructed as follow:

Ile463, Ala481, Lys483, Glu501, Leu505, Phe516, Ile527, Gln530, Trp531, Cys532, Ser535, Ser536, His539, Phe582, Phe583, Asp594 and Phe595.

2.3.6. QTAIM calculations (Molecular interactions (MI)).

Topological analysis of the electron density constitutes a powerful tool to evaluate the electronic properties of the molecular systems of biological interest and allows for a deep examination of the molecular interactions. This methodology has been successfully applied in the study of the properties of a variety of conventional and unconventional HBs, aromatic HBs, and π-π stacking [42–44]. A very important point is that from the QTAIM, it is possible to determine in an unequivocal way the different strong and weak interactions between two atoms observing the existence of bond critical points (BCPs) and their respective bond paths. It should be noted that this detailed analysis is not possible from the evaluation of the geometrical parameters (bond, distance and angles).

Here, we only present the essential theoretical information that is needed for the understanding of the QTAIM calculations performed in our study because the use of topological concepts in the description of intra/intermolecular interactions is well documented in the standard literature [45–48]. More details about these types of calculations can be obtained from references [49,50].

Charge density topological analysis based in the QTAIM was performed on the different reduced models to evaluate the L–R interactions. These calculations were performed with the help of MultiwfnandAIMAllsoftware [51,52]. The wave function used as input for these calculations were computed with the Gaussian 16 package [53] by employing the B3LYP functional [38,54,55], with dispersion correction (B3LYP-D [56]), and 6-31G(d) as a basis set. The empirical dispersion correction for the B3LYP functional was applied by invoking the IOp 3/124 = 3 keyword in Gaussian 16. The topological properties of a scalar field such as ρ(r) are summarized in terms of their critical points, i.e., the points where $\Delta\rho(r) = 0$. Critical points are classified according to their type (ω, σ) by stating their rank, ω, and signature, σ. The rank is equal to the number of nonzero eigenvalues of the Hessian matrix of ρ(r) at rc, while the signature is the algebraic sum of the signs of the eigenvalues of this matrix. Critical points of (3, −1) and (3, +1) type describe saddle points, while the (3, −3) is a maximum and (3, +3) is a minimum in the field. Among these critical points, the (3, −1) or bond critical points are the most relevant ones since they are found between any two atoms linked by a chemical bond.

2.3.7. Some concepts useful in theory of atoms in molecules

The electron charge density, ρ(r), is a physical quantity that has a definite value at each point in space. QTAIM analysis is based on the critical points (CPs) of this electronic density distribution. The gradient vector of the charge density (Δρ(r)) vanishes at these points, which are characterized by the three eigenvalues (λ1, λ2, and λ3) of the Hessian matrix of the charge density. In the topological distribution of the electronic charge density, three topological features or elements appear as a consequence of the interaction between two atoms: (a) a bond critical point (BCP), (b) a bond path (BP), and (c) an interatomic surface (IAS). A BCP has two negative eigenvalues and a positive eigenvalue. The two negative eigenvalues of the Hessian matrix (λ1 and λ2) measure the degree of contraction of the charge density at BCP (ρ(r)) perpendicular to the bond toward the critical point, while the positive eigenvalue (λ3) measures the degree of contraction parallel to the bond and from the BCP toward each of the neighboring nuclei. As mentioned above, the eigenvectors associated with the eigenvalue λ3 define a unique pair of trajectories of Δρ(r) that originate in the (3, −1) BCP, each of which terminates at the nucleus of one of the neighboring atoms (3, −3). This pair of trajectories defines a line through space along which the electron density is a maximum with respect to any neighboring line forming an atomic interaction line (AIL) or bond path. Each bond path is homeomorphically mirrored by a virial path, a line of maximum negative potential energy density linking the same nuclei. Thus, the presence of a bond path and its associated virial path provides a universal indicator of bonding between the atoms so linked. Three other critical point types can be defined in the topology of ρ(r): (3, +1) or the ring critical point, RCP; (3, −3) or the nuclear critical point, NCP, associated with the nuclei; and (3, +3) or the cage critical point, CCP. This last CP type appears when several rings topologically describe a cage.

3. Results and discussion

3.1. Synthesis of compounds 13, 14 and 26–31

Studied 1-[3-(4-substituted-benzoyloxy)-2-hydroxypropyl]-4-phenylpiperazin-1-ium chlorides **3–8** were prepared by multiple-step synthesis described recently [26–28]. New compounds **13**, **14** as well as **26–31** were prepared according to Scheme 1 similarly as previously described anilides**9–12**, **15–25** [29–33]. Briefly, the condensation of naphthalenecarboxylic acid with appropriate ring-substituted aniline using phosphorus trichloride in dry chlorobenzene under microwave conditions gave a target substituted *N*-arylnaphthalene-carboxanilides**13**, **14**, **26–31**.

3.2. Biological assays

3.2.1. Substituted piperazinylethanols and substituted piperazinylpropandiols (compounds 3–8)

We have recently reported compounds **3** and **22** (Fig. 1) as potential inhibitors of BRAF [25]. These compounds were obtained from a virtual screening investigation. In the present study, we have taken these two molecules as starting structures for the search of new BRAF inhibitors. First, we evaluated analogues of compound **3** and therefore we use the previously reported compounds **4–8.** Note that these compounds are closely related to compound **3** in which structural changes had been

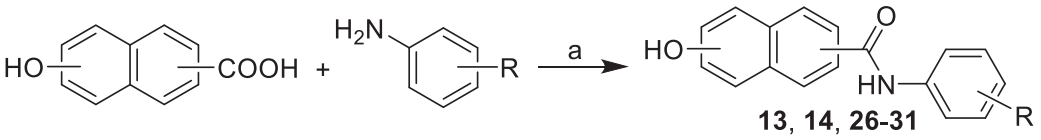

Scheme1. Synthesis of ring-substituted naphthalene-carboxanilides**13**, **14**, **26–31**: (a) PCl3, chlorobenzene, microwave irradiation (MW) [29–33].

introduced at both extremes of the molecule. Therefore, these compounds fit very well for our purposes. Our next step was to determine the phosphorylation of ERK in Lu1205 cells treated with these new compounds at 10 μM for 2 h by western blot. It is important to note that these bioassays do not categorically guarantee that the compounds have direct effects on BRAF; they allow making an extrapolation based on the levels of ERK phosphorylation, which is a downstream target of BRAF. Although an additional support to the possible effect on BRAF are the results obtained from molecular modeling simulations; specific BRAF activity determination is required to clearly confirm the effect of the compounds on BRAF.

Although all compounds reduce significantly ERK phosphorylation at concentrations of 10 μM (see Fig. 2**A**), only compound 5 showed an inhibitory effect at lower concentration (1 μM) (see **figure S1A** as supporting information). In parallel, we evaluated the effects of these compounds in cellular viability. Our results showed that none of these compounds have a significant effect on cell viability at concentrations of 10 μM or 1 μM (Fig. 2**B and S1B**). Based on these results, we decided to focus our efforts on the other compounds reported here, the hydroxynaphthalenecarboxamides derivatives.

3.2.2. Substituted hydroxynaphthalenecarboxamides (compounds 9–25)

To find new inhibitors with this structural scaffold, we decided to take our previously reported compound **22** as the starting structure. Our research group has previously published different compounds structurally related to **22**. They are compounds **9–11** (type C1, Fig. 1 [29]), **12–14** (type *C*2, Fig. 1 [30]), **15–17** (type C3, Fig. 1 [31]), **18** and **19** (type C4, Fig. 1 [32]) and compounds **20–25** (type C5, Fig. 1 [33]). It must be pointed out that compounds **13** and **14** were synthesized exclusively for this study and therefore they are described here for the first time; the rest of the compounds have been previously reported as indicated. Taking the advantage of having these compounds available in our laboratory, we determined their potential inhibitory activities. It is important to highlight that compound **22** has been recently reported in our previous article [25], however it was evaluated once again as a positive control, to verify the reliability of our bioassays. Compounds used in this study were selected in such a way that they allow us to evaluate at least two different aspects from the structural point of view of the ligand: a) presence and position of the OH group at the naphthalene moiety; b) type and position of substituents in the benzene group.

Fig. 3 shows the results obtained for the phosphorylation of ERK in Lu1205 cells treated with compounds **9–25** at 10 μM for 2 h by western blot. These results clearly show that only compounds **20–25** (type C5) significantly reduce ERK phosphorylation at concentrations of 10 μM. The rest of the tested compounds did not show significant activities.

Altogether, these data suggest several conclusions from the structural point of view of the ligand. The lack of activity obtained for compounds **9–11** shows that the presence of the OH group at the naphthalene moiety might be important for the inhibitory effect in these compounds; however the lack of activity of compounds **12–19** clearly indicates that not only the presence of an OH group is necessary, but its spatial position appears to be important. It should be noted that compounds **12–19** have the OH group in different positions at the naphthalene moiety and none of them showed significant inhibitory effect at 10 μM. Moreover, the presence of a substituent with

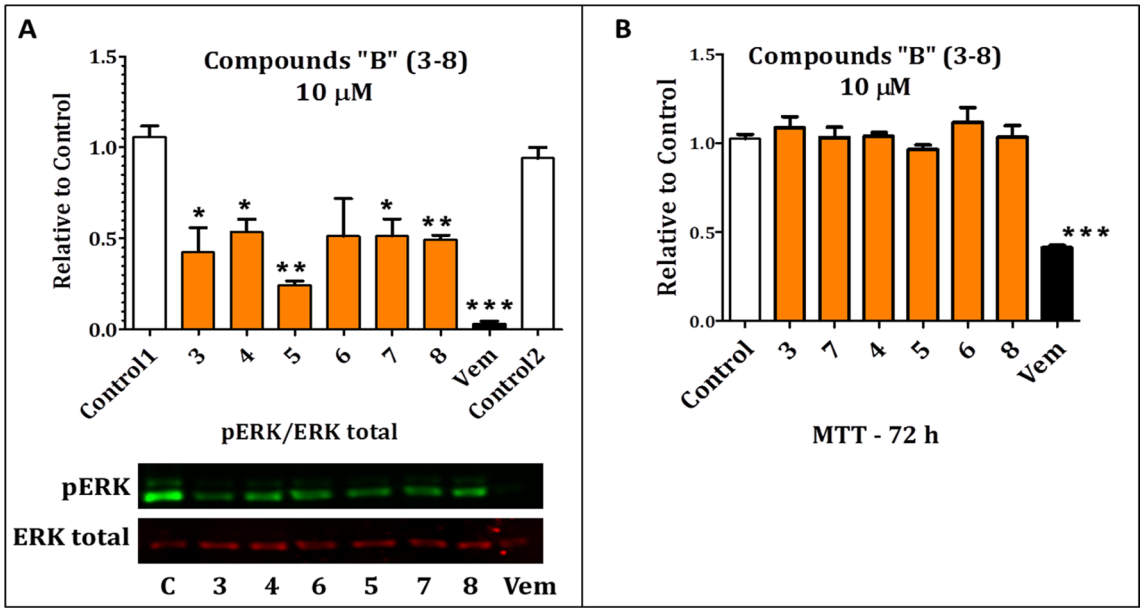

Fig. 2. Lu1205 melanoma cells were treated with compounds type B (**3–8**, orange bars), control (carrier DMSO, white bars) or Vemurafenib (Vem, black bars) at 10 μM for 2 h (**A**) or 72 h (**B**). **A)** Proteins from the cell lysates were separated by SDS-PAGE and then western blot was performed by using specific antibodies against pERK and ERK total. Image Studio 5.2 was used to make the quantification of each band and establish the relation pERK/ERK total respect to the control. A representative western blot is shown. **B)** Cell viability was determined by the reduction of the MTT reagent. Crystals were dissolved in DMSO and absorbance was measured at 540 nm in the spectrophotometer. Absorbance of each treatment was normalized to the Absorbance of the control. The results are shown as the mean ± SEM of 3 independent experiments. Statistics: One-way ANOVA and Tukey post-test (*$p < 0.05$; **$p < 0.01$; ***$p < 0.001$). (For interpretation of the references to colour in this figure legend, the reader is referred to the web version of this article.)

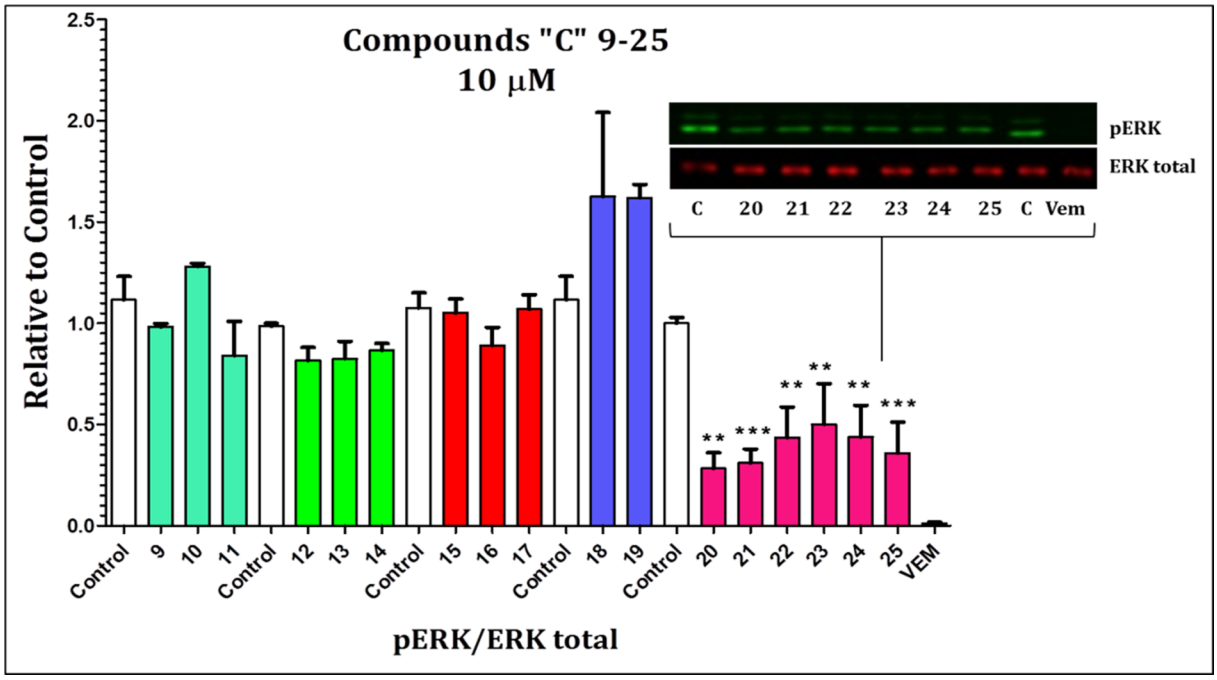

Fig. 3. Lu1205 melanoma cells were treated with compounds "C" **9–25** (C1 cyan bars; *C*2 green bars; C3 red bars; C4 blue bars; C5 pink bars), control (carrier DMSO, white bars) or Vemurafenib (black bars) at 10 μM for 2 h. Proteins from the cell lysates were separated by SDS-PAGE and then immunoblot was performed by using pERK and ERK total specific antibodies. Image Studio 5.2 was used to make the quantification of each band and establish the relation pERK/ERK total respect to the control. The results are shown as the mean ± SEM of 3 independent experiments. Statistics: One-way ANOVA and Tukey post-test (*p < 0.05; **p < 0.01; ***p < 0.001). A representative western blot of active compounds 20–25 is shown. (For interpretation of the references to colour in this figure legend, the reader is referred to the web version of this article.)

electronegative characteristics (such as Br or CF_3) might improve the activity of these series of compounds. Certainly, all the active compounds possess substituents with those characteristics at the benzene ring (type C5, compounds**20-25**).Considering that only compounds **20–25** did show inhibitory effect, they were also tested at 1 μM. Remarkably, all these compounds reduced ERK phosphorylation at this concentration (Fig. 4**A**) but only compounds **21** and **22** also reduced significantly cell viability of Lu1205 melanoma cells (Fig. 4**B**). These data suggest that they are potential new anti-carcinogenic agents.

3.3. Molecular modeling study

In order to understand more deeply our experimental results, a molecular modeling study was developed. We carried out this study in four steps using different modeling techniques. First, we conducted a docking study; in the second step we performed simulations using molecular dynamics calculations. With these data we performed an analysis by residue and lastly, quantum mechanics calculations were made to evaluate in detail the molecular interactions that stabilize the different ligand-receptor complexes.

As expected, the docking study indicates that compound **21** is bound in a spatial arrangement in a similar fashion to that previously reported for compound **22** [25]. It should be noted that Vemurafenib displays a similar spatial ordering as well (Fig. 5 [25]).

Molecular dynamics calculations allowed us to perform an analysis per residue for the different series of compounds to understand the biological results obtained for these compounds. The histogram obtained for compound **21** is shown in Fig. 6**A**.The interactions of compound **21** are mainly with Asp594 and Lys483 (slightly less with the last one). The other interactions that stabilize the formation of this complex are noticeably more weak (Ile463, Val471, Ala481, Thr529 and Phe583). It is important to highlight the high similarity between the histograms of compound 21 and Vemurafenib (see Fig. 6**A and 6B**). In fact, considering just these simulations, we could expect that compound **21** would show the same inhibitory effect as Vemurafenib, however its activity, although significant, is much lower. In the next section, we explore a possible explanation for this performance by carrying out a more detailed analysis of the molecular interactions.

Histograms obtained for compounds **10** and **18** are shown in Fig. 6**C and 6D,** respectively. These histograms emphasize the clear differences between active compounds (Fig. 6**A and B**) from those with marginal activity or inactive (compounds **9–19**, Fig. 6**C and D**).

Although the interactions observed for these inactive compounds**10** and **18** are almost the same to those obtained for compound **21** and Vemurafenib, such interactions are markedly weaker. Note that most of these interactions do not reach 2 Kcal/mol and none of them reach 3.8 Kcal/mol. In particular, those interactions with Asp594 and Lys483 are significantly weaker compared to the observed in active compounds. These results are in agreement with our experimental data. Similar histograms were obtained for the rest of the inactive compounds (data not shown). In order to better understand the behavior of ligands, we have recently shown that it is helpful to analyze the molecular interactions of the different complexes employing more accurate calculations. For this purpose, combined MD/QTAIM (quantum theory of atoms in molecules) calculations are extremely useful for detailing the molecular interactions of different ligand-receptor complexes [49,50]. Therefore, we perform a QTAIM analysis for the most representative complexes of these compounds.

3.4. Topological analysis of the charge density

QTAIM analysis consists in the mapping of the gradient vector field ∇ on top of the charge density (ρ) of the system to give rise to the topological elements of the charge density, two of which we are mainly concerned in here: the Bond Critical Points (BCPs) at the complex intermolecular interface and the Bond Paths (BPs) that connect the BCP to bonded atoms of the ligand and the protein. Unlike the geometrical parameters (i.e. bond distance and angle and also types of atoms

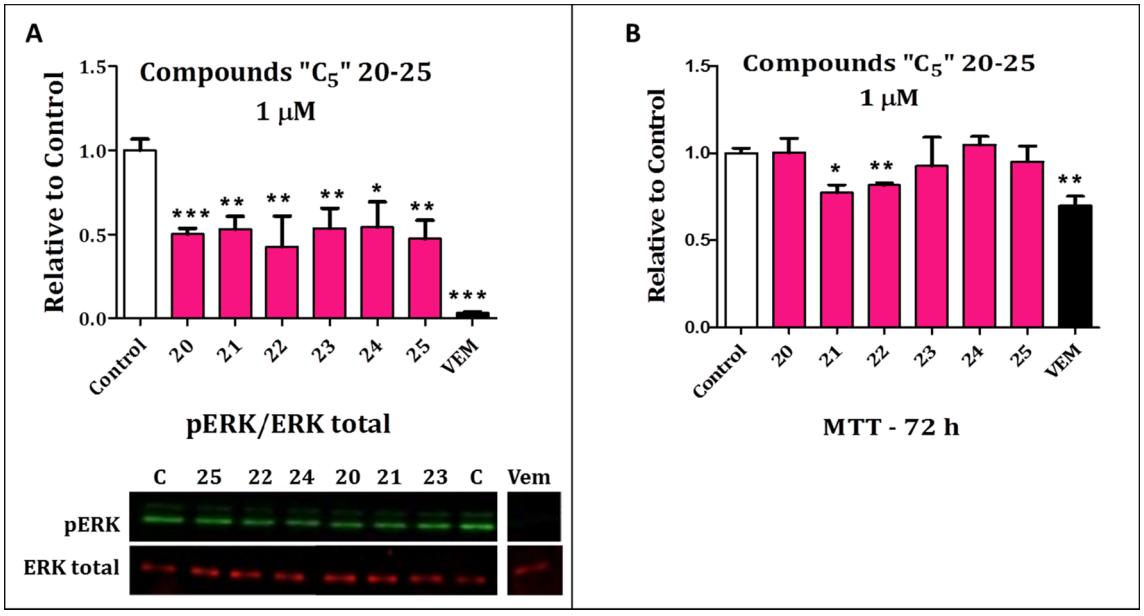

Fig. 4. Lu1205 melanoma cells were treated with compounds "C_5" **20–25** (pink bars), control (carrier DMSO, white bars) or Vemurafenib (black bars) at 1 μM for 2 h **(A)** or 72 h **(B)**. **A)** Proteins from the cell lysates were separated by SDS-PAGE and then immunoblot was performed by using specific antibodies against pERK and ERK total. Image Studio 5.2 was used to make the quantification of each band and establish the relation pERK/ERK total respect to the control. A representative western blot is shown. **B)** MTT reagent was added and incubated 3 h additionally. Formazan crystals were dissolved in DMSO and absorbance was measured at 540 nm. Each treatment was normalized to the control. The results are shown as the mean ± SEM of 3 independent experiments. Statistics: One-way ANOVA and Tukey post-test (*$p < 0.05$; **$p < 0.01$; ***$p < 0.001$). (For interpretation of the references to colour in this figure legend, the reader is referred to the web version of this article.)

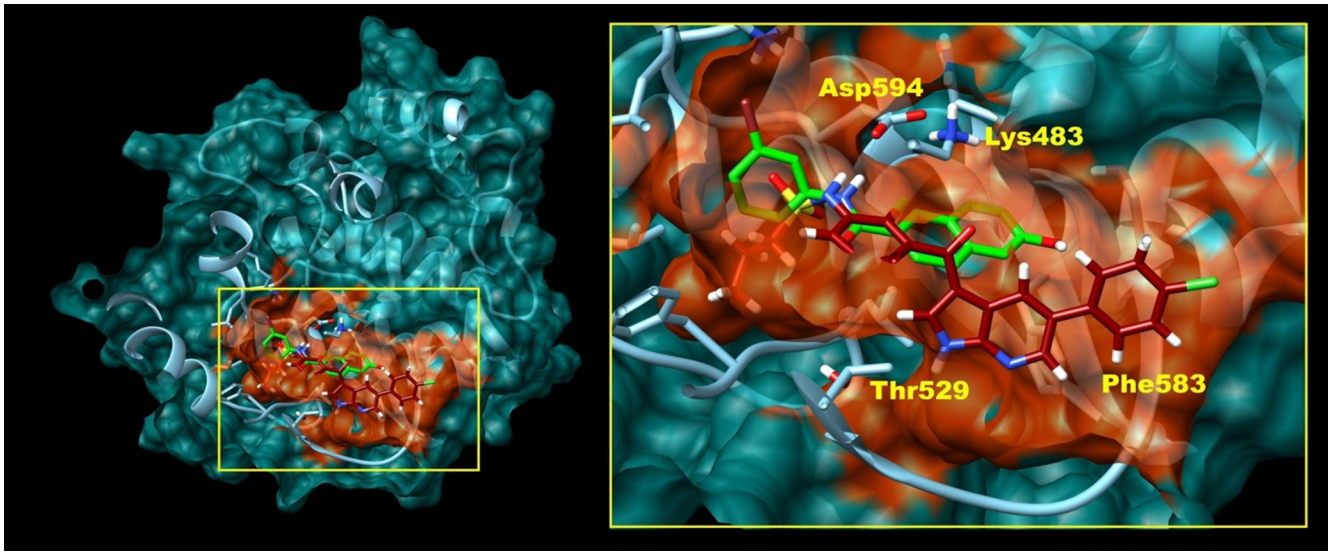

Fig. 5. Spatial view of the ordering adopted by compound **21** (green) and Vemurafenib (dark red) in the active site of BRAF. (For interpretation of the references to colour in this figure legend, the reader is referred to the web version of this article.)

involved) for describing non covalent interactions, QTAIM does not rely on any arbitrary criteria for deciding whether an interaction is actually formed or not: the sole presence of a BCP and the corresponding BPs between two atoms guarantee the existence of the interaction. Conversely, if no BCP and BPs is observed, then it is a fact that those atoms are not interacting with each other. Therefore, QTAIM allows detecting weak intermolecular interactions, mostly involving hydrophobic moieties which lack of well-defined geometrical limits.

Fig. 7 depicts the charge density molecular graph of compound **21** bound to BRAF.

As shown in Fig. 7, an intricate network of interactions holds compound **21** within the binding cleft of the enzyme. Since the charge density value at the BCP of the interaction is a measure of the strength of that interaction, the sum of charge density values for all the intermolecular interactions gives an estimate of the overall strength of the binding. Similarly, the sum of charge density values corresponding to all the interactions of a particular functional group of the ligand with enzyme atoms is a measure of the anchoring of that group to the binding cleft.

Bar plot in Fig. 8 shows the charge density sum corresponding to interactions of Vemurafenib and compound **21** with BRAF. As expected, Vemurafenib is anchored to the BRAF binding cleft several times more strongly than compound **21**, a finding that correlates very well with results of the ERK phosphorylation assays discussed above.

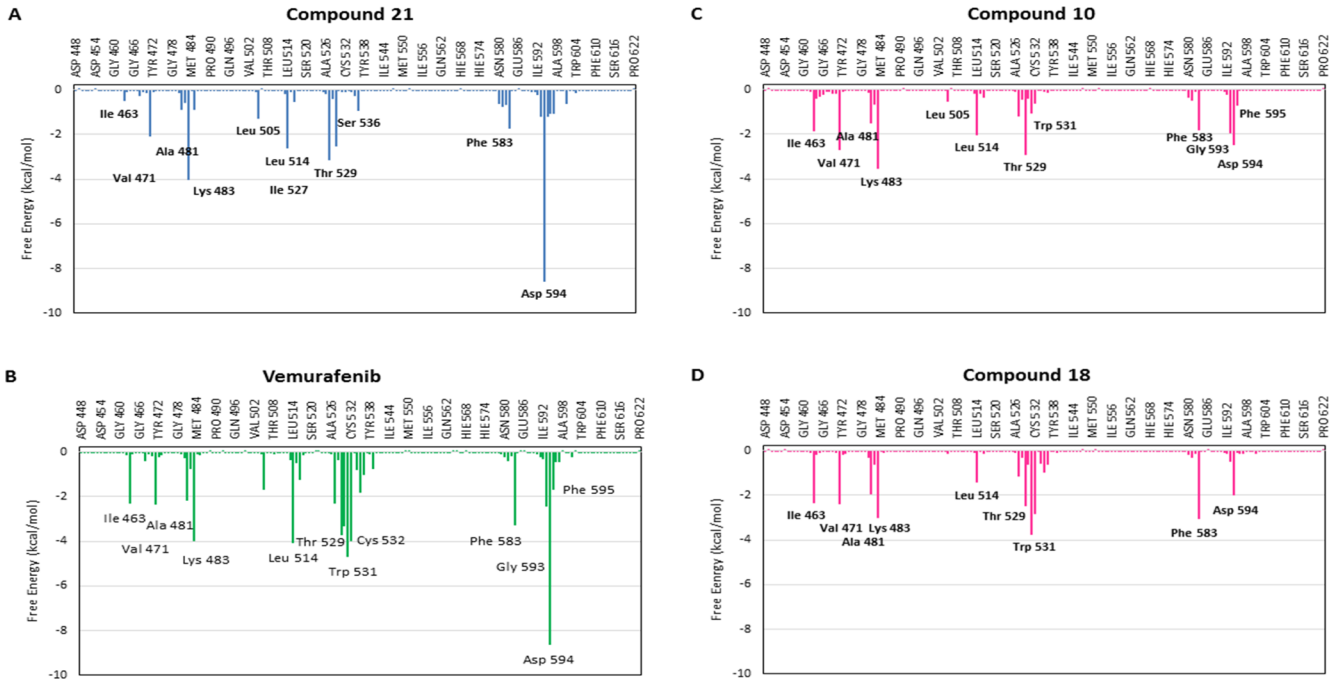

Fig. 6. Histograms for compounds **21** (**A**), Vemurafenib (**B**), 10 (**C**) and 18 (**D**) show the interaction energies with the main amino acids that participate in the formation of the complex enzyme-ligand.

Furthermore, Vemurafenib binds more strongly than compound **21** to both regions of the enzyme, i.e. DFG loop as well as the hinge region. Figure S2 shows a superposition of the binding modes of compound **21**, Vemurafenib (PDB code = 3OG7) and a very close analog of ATP (PDB code = 6U2G).

It is clearly visible the Y-shaped bifurcated binding cleft of BRAF in which ATP analog shares with compound **21** and Vemurafenib the same binding site on the Hinge region. However they target different sides of the binding cleft bifurcation around the DFG loop region. As can be seen, both Vemurafenib and compound **21** target a deep pocket that remains unexplored by ATP enzyme substrate.

Despite the quite similar binding mode of Vemurafenib and

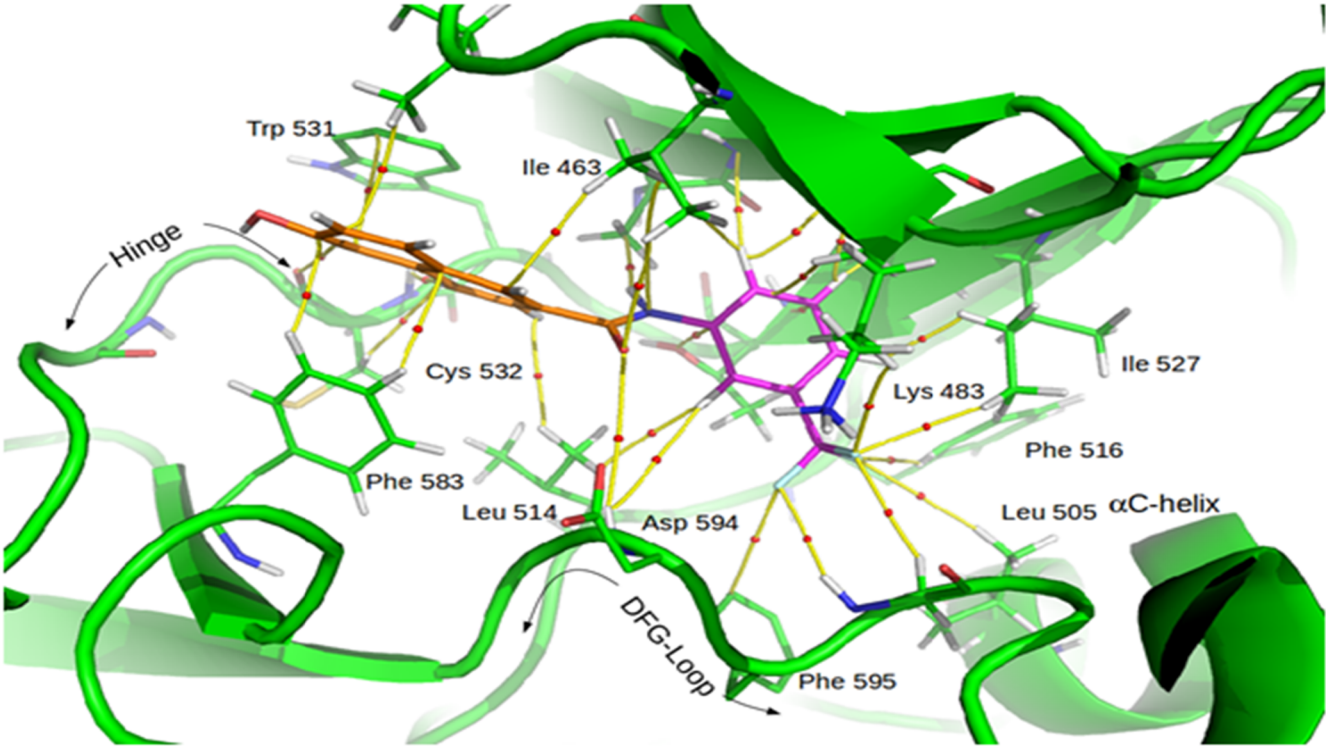

Fig. 7. Charge density molecular graph of compound **21** bound to BRAF. BCPs and BPs for the complex intermolecular interactions are shown in red spheres and yellow lines, respectively. The interacting parts of compound **21** with DFG-loop and Hinge are colored in purple and orange, respectively. (For interpretation of the references to colour in this figure legend, the reader is referred to the web version of this article.)

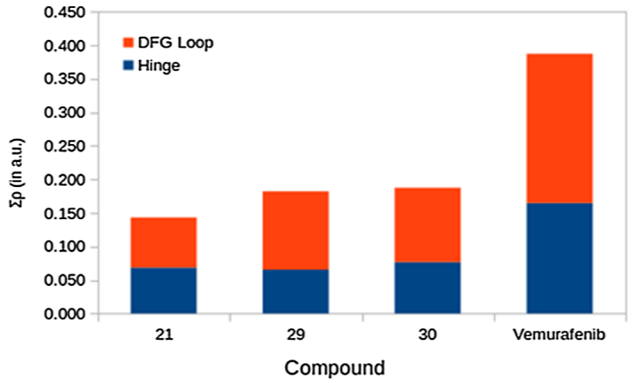

Fig. 8. Charge density sum (Σρ) for interactions of Vemurafenib and compounds**21, 29** and **30** with BRAF. Total charge density sum (i.e. full height of stacked bars) is decomposed in interactions with the Hinge and DFG loop regions of BRAF binding cleft. Results obtained for compounds **29** and **30** are shown here but they are discussed in *section 3.5*.

compound **21**, the first one is able to form much stronger interactions than compound **21**, as evidenced by the bar plot in Fig. 8. Accordingly, in what follows we discuss the differences in the intermolecular interactions profiles of both inhibitors to uncover such differences. To help in the discussion, we have included the molecular graph of Vemurafenib at the BRAF binding cleft (**Figure S3**). A very similar graph has been reported by us in Campos, *et al* [25]. We have recalculated this complex using the same methodology employed here to homogenize the results. However, it should be noted that the results obtained are closely related to those previously reported. By comparing the molecular graphs in **Figure 7 and S3** one can see that the residues involved in the binding of compound **21** and Vemurafenib are basically the same.

Fig. 9 shows the intermolecular interaction profiles for complexes of BRAF with compound **21** and Vemurafenib.

While residues involved in the anchoring of both compounds are almost the same as argued above, there are significant differences in quantitative terms, namely several of the involved residues interact much more strongly with Vemurafenib than with compound **21**. This is particularly true for interactions with key residue Asp594 from DFG loop and also with Gln530 and Cys532 from the hinge loop. Additionally, Vemurafenib forms other interactions with hinge residues like Gly534, Ser535 and His539 that are not formed for compound **21**.

Moreover, residues Lys483 and Phe468 from β-sheet motif that conform the roof of the binding cleft are strongly interacting with Vemurafenib while only forms weak contacts with compound **21** (i.e. as in the case of Lys483) or do not interact at all with it (i.e. as in the case of Phe468). These last interactions help to keep β-sheet motif close to the DFG loop thus allowing formation of salt bridge between Lys483 and Asp594 which in turn stabilizes the DFG-in/α-helix- out conformation of BRAF when it is bound to Vemurafenib.

On the other hand, as compound **21** is not able to form stable interactions with residue Phe468 and Lys483, the β-sheet motif moves away from the DFG loop and the salt bridge between Lys483 and Asn594 gets broken. Salt bridge disruption together with the fact that compound **21** only interacts weakly with DFG loop residues like Asp594 suggest that this loop could move quite freely between in and out conformation of BRAF. Thus, we hypothesize that if we were able to simulate complex of BRAF with compound **21** for long enough time in the microsecond/millisecond time scale, DFG loop would move from in to out conformation and compound **21** would eventually end up expelled from BRAF binding cleft in this process. In contrast, in the case of Vemurafenib, this conformational transition should take more time to occur (if it actually does at all) because the DFG loop is more tightly hold in the DFG-in conformation by direct interactions with the inhibitor as well as by the salt bridge with Lys483.

3.5. Bi-substituted hydroxynaphthalenecarboxamides (compounds 26–31)

At this stage of our study and based on our results obtained from molecular modeling, we wondering if bi-substituted compounds could have any advantage compared to the mono-substituted derivatives. The simulations previously shown indicate that BRAF binding site has enough space to properly accommodate another substituent on the benzene ring of the inhibitors. Thus, we decided to perform a molecular modeling study for bi-substituted derivatives. To this end, we selected compounds that had bromine atom and trifluoromethyl substituents at different spatial positions.

The histograms obtained for bi-substituted derivatives are shown in **Figure S4**. It can be clearly seen that histograms of compounds **29** and **30** have a very similar profile to those obtained for compound **21** and Vemurafenib (compare **Figures S2D-E** with **6A** and **6B**).Similar histograms were obtained for compounds **26, 27, 28** and **31** which are shown in **Figure S2** as supporting information.

Furthermore, MD/QTAIM study revealed very interesting results for these compounds. For instance, the total ρ(r) values obtained for

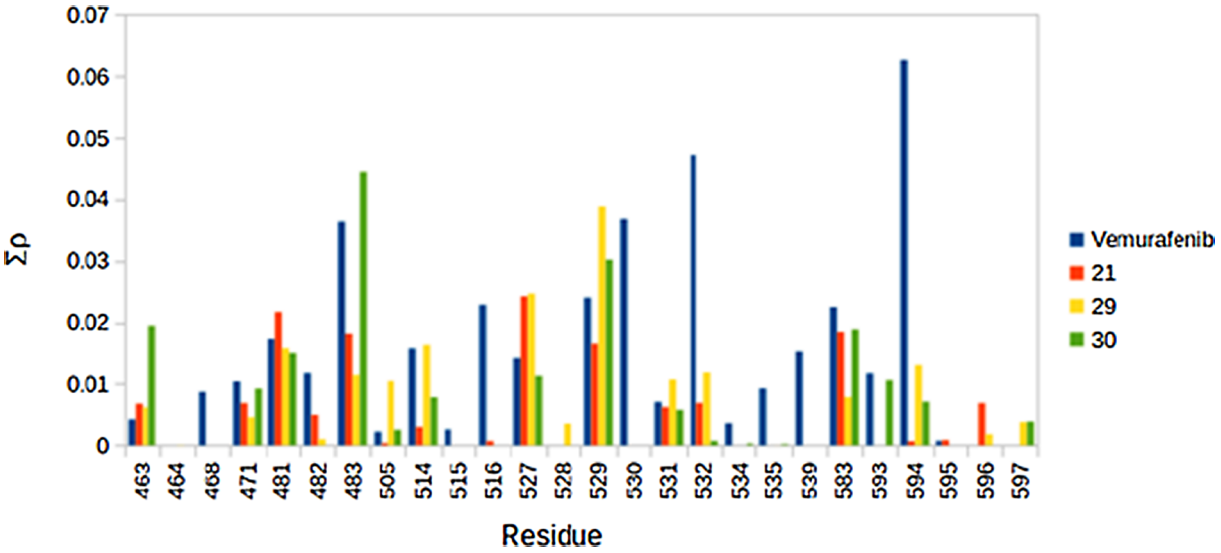

Fig. 9. Per-residue charge density sum (in atomic units) of the intermolecular interactions in complexes of BRAF with compounds **21**, **29**, **30** and Vemurafenib. Results obtained for compounds **29** and **30** are shown here but they are discussed in *section 3.5*.

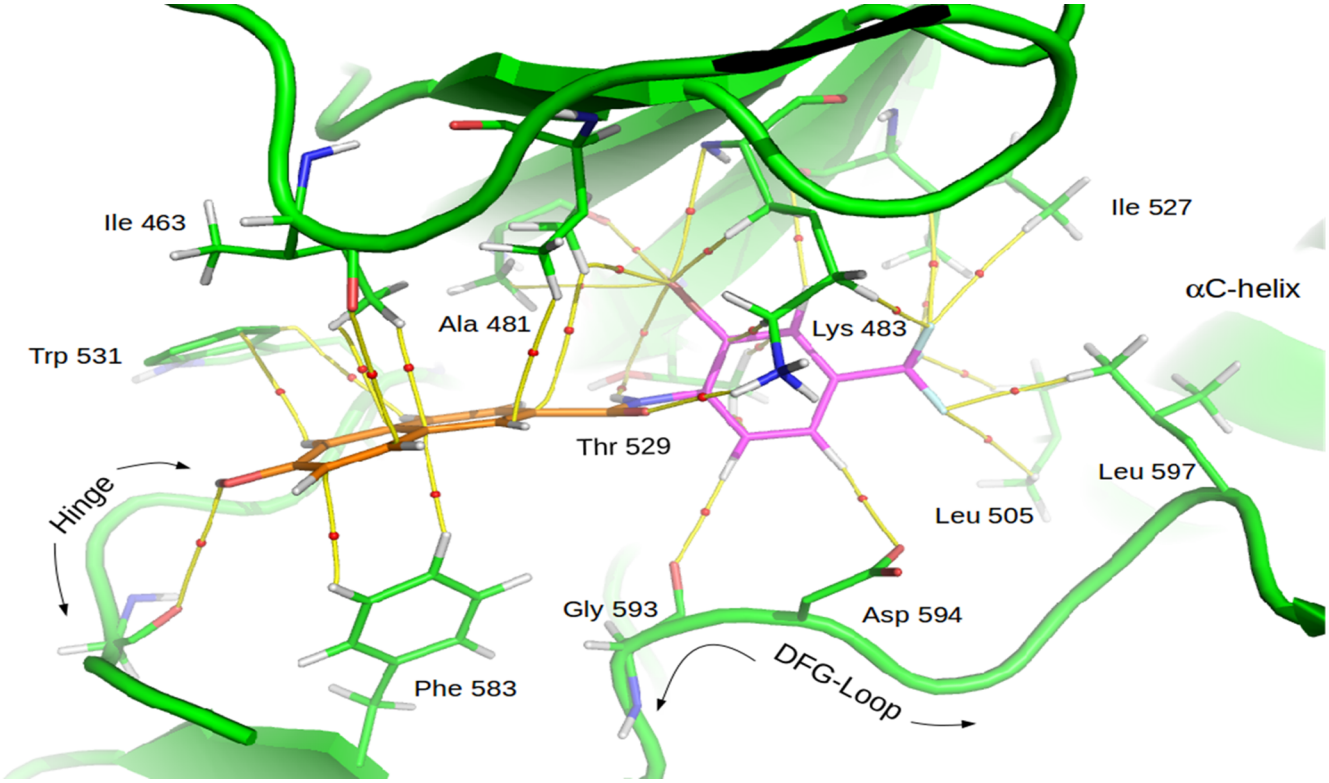

Fig. 10. Charge density molecular graph of compound **30** bound to BRAF. BCPs and BPs for the complex intermolecular interactions are shown in red spheres and yellow lines, respectively. The interacting parts of compound **30** with DFG-loop and Hinge are colored in purple and orange, respectively. (For interpretation of the references to colour in this figure legend, the reader is referred to the web version of this article.)

compounds **29** and **30** are slightly higher than those of **21** but at the same time lower than those of Vemurafenib (Fig. 8). An interesting point to remark is that the blue portion of compounds **29** and **30** is almost the same as that of compound **21**, however the red portion of bi-substituted compounds is higher compared to **21** (see Fig. 8). This is expected since the increased interaction in this portion of the molecule is due to the interactions produced by the two groups included in the benzene ring. This can be better observed in Fig. 10 in which these interactions have been analyzed residue by residue. The strongest interactions of Vemurafenib with respect to compounds **29** and **30** can also be clearly seen in this figure. Simulations and calculations were performed for six compounds (**26–31**) although only the results of **29** and **30** are shown here by a space issue.

Compound **30** shows a binding mode very similar to that of compound **21** at BRAF binding cleft. Actually, structural superposition of both complexes shows that, except for the substituents at the benzene rings, ligand atoms are almost perfectly superimposed (data not shown). In other words, the incorporation of a second substituent on the benzene ring significantly increases the anchoring of compound **30** but without affecting its overall binding mode. This finding is further supported by Fig. 8, which shows that the binding to BRAF hinge region through the ligand hydroxynaphtyl group is not affected by number and position of substituents. However, the anchoring at the DFG loop region does increase markedly upon the incorporation of a second substituent. The increase in anchoring strength of compound **30** as compared to compound **21** is related to the greater number of interactions that both substituents can achieve together.

As can be seen in the molecular graph of Fig. 10, there are several bond paths connecting the bromine atom at benzene ring to residues Ala481, Lys483 and Thr529 from the β-sheet motif. At the same time, the trifluoromethyl substituent fills the hydrophobic pocket originated by the outward shift of the αC-helix where it forms several hydrophobic interactions with residues Leu505, Ile527 and Leu597. To better understand the conformational changes that take place in the binding site, we construct **Figure S6** which shows a superposition of BRAF bound to compounds **21**, **30** and Vemurafenib as well as BRAF in DFG-out conformation. Based on these results, we decided to synthesize and measure the biological activity of these six compounds.

3.5.1. *Experimental corroboration*

Based on the results discussed in the previous section, our next step was to synthesize and evaluate the six new bi-substituted derivatives (compounds **26–31**). Details of synthesis were discussed in *section 3.1.* Notably, all these new compounds showed significant inhibitory activity on BRAF (see Fig. 11**A and S5A**). In fact, these compounds not only showed a significant inhibitory effect on BRAF at both concentrations tested (10 and 1 μM), but also reduced viability of Lu1205 melanoma cells (see Fig. 11**B and S5B**).

It is important to remark that these compounds displayed stronger activities in comparison to compound **21** and those previously reported [25]. Moreover, these results constitute an additional support to our molecular modeling study since they are in complete agreement with their predictions. These compounds, although showing less activity than Vemurafenib, are more active than compound **21** and the other mono-substituted compounds in the series.

4. Conclusions

Recently, we reported two new structural scaffolds as potential inhibitors of BRAF; both series of compounds were studied in greater depth in the present work. Our results indicate that structural analogues of the previously reported compound **3** do not show significantly better activities to that previously reported for this compound which was chosen as starting structure. In contrast, the results obtained for hydroxynaphthalenecarboxamides were more successful. We report here new compounds possessing this structural scaffold with significant

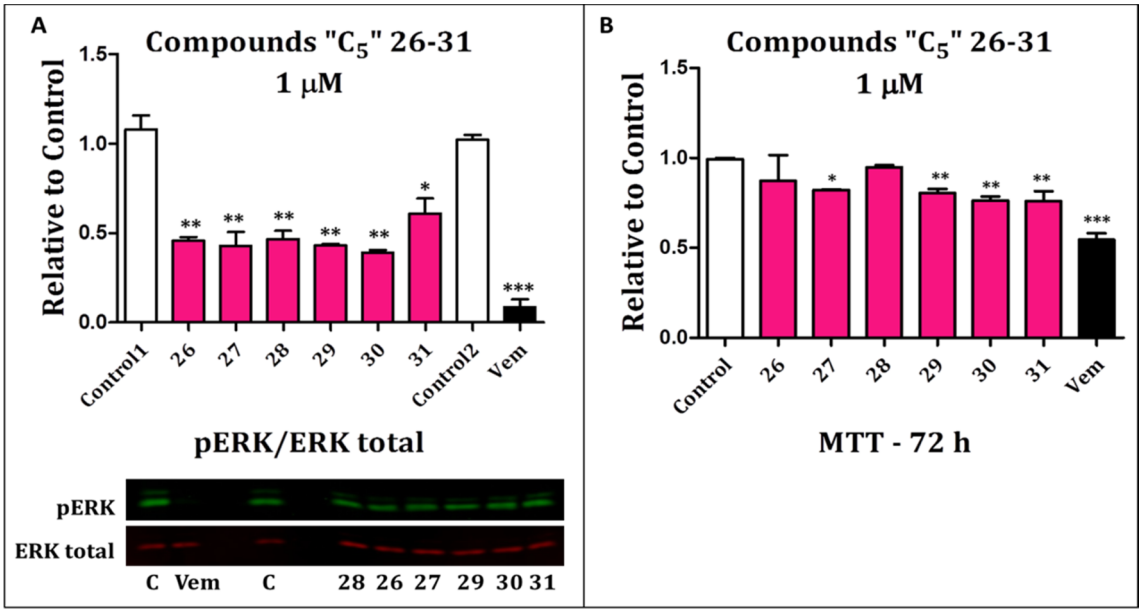

Fig. 11. Lu1205 melanoma cells were treated with compounds "C_5" **26–31** (pink bars), control (carrier DMSO, white bars) or Vemurafenib (Vem, black bars) at 1 μM for 2 h **(A)** or 72 h **(B)**. **A)** Proteins from the cell lysates were separated by SDS-PAGE and then immunoblot was performed by using specific antibodies against pERK and ERK total. Image Studio 5.2 was used to make the quantification of each band and establish the relation pERK/ERK total respect to the control. A representative western blot is shown. **B)** MTT reagent was added and incubated for 3 additional hours. DMSO was employed to dissolve the formazan crystals and the absorbance was measured at 540 nm. Each treatment was normalized to the control. The results are shown as the mean ± SEM of 3 independent experiments. Statistics: One-way ANOVA and Tukey post-test (*p < 0.05; **p < 0.01; ***p < 0.001).

inhibitory activity on BRAF. Among these derivatives, compounds **21, 22** and six new bi-substituted derivatives (**26–31**) are those that showed the strongest inhibitory activities. In addition, these compounds also reduce notably the cell viability of Lu1205 melanoma cells and therefore they are good candidates for further development. In the same line, bi-substituted compounds seem to have structural advantages with respect to the mono-substituted analogues.

In order to better understand these experimental results, we carried out a molecular modeling study using different combined techniques. While simulations using simple techniques such as docking and MD simulations allowed us to explain which the best structural scaffold is, such results are not appropriate to explain why some compounds within the same series displayed different activities. These explanations were obtained from the combined MD/QTAIM calculations that allowed us to explain in detail the molecular interactions that stabilize the different molecular complexes reported here.

On the other hand, QTAIM results of the new compounds are in agreement to those observed for Vemurafenib, explaining the lower activity obtained for the compounds reported here with respect to the drug used as reference. This structural information is important for the design and development of new BRAF inhibitors possessing this type of structural scaffold.

Declaration of Competing Interest

The authors declare that they have no known competing financial interests or personal relationships that could have appeared to influence the work reported in this paper.

Acknowledgements

This work was supported by grants from INC (Instituto Nacional del Cáncer-Argentina) to R.D.E., ANPCyT-Argentina PICT 2378-2014 to S.E.A. and CONICET, Argentina PIP916-2015 to S.E.A. Grants from Universidad Nacional de San Luis (UNSL-Argentina) partially supported this work. Dr. Ludmila Campos is a postdoctoral fellowship of CONICET-Argentina. This work was also partially supported by the Ministry of Education of the Czech Republic (LO1305) and Palacky University in Olomouc (IGA_PrF_2020_023). M.O. was supported by SustES (CZ.02.1.01/0.0/0.0/16_019/0000797). We thank Dr. Pablo Bergami (Universidad de Maimónides, Buenos Aires) for generously provide us Lu1205 melanoma cell line.

Appendix A. Supplementary data

Supplementary data to this article can be found online at https://doi.org/10.1016/j.bioorg.2020.104145.

References

[1] H. Davies Y et al, Mutations of the BRAF gene in human cancer, Nature, pp. 949-54, 2002.
[2] M.L. Turski, S.J. Vidwans, F. Janku, I. Garrido-Laguna, J. Munoz, R. Schwab, V. Subbiah, J. Rodon, R. Kurzrock, Genomically Driven Tumors and Actionability across Histologies: BRAF-Mutant Cancers as a Paradigm, Molecular Cancer Therapeutics 15 (4) (2016) 533–547, https://doi.org/10.1158/1535-7163.MCT-15-0643.
[3] K. Young, A. Minchom, Y.J. Larkin, BRIM-1, -2 and -3 Trials: Improved Survival With Vemurafenib in Metastatic Melanoma Patients With a BRAF(V600E) Mutation, Future Oncol., pp. 499-507, 2012.
[4] J.J. Luke, K.T. Flaherty, A. Ribas, Y.G.V. Long, Targeted agents and immunotherapies: optimizing outcomes in melanoma, Nat. Rev. Clin. Oncol. (2017) 463–482.
[5] S.J. Welsh, H. Rizos, R.A. Scolyer, Y.G.V. Long, Resistance to combination BRAF and MEK inhibition in metastatic melanoma: Where to next? European Journal of Cancer (2016) 76–85.
[6] D. Barras, BRAF Mutation in Colorectal Cancer: An Update., *Biomark*, Cancer. (2015) 9–12.
[7] K. B. Kim, M. E. Cabanillas, A. J. Lazar, Y.S. I. Sherman, Clinical Responses to Vemurafenib in Patients with Metastatic Papillary Thyroid Cancer Harboring BRAFV600E Mutation, Thyroid, p. 1277–1283, 2013.
[8] R. Dummer, P. A. Ascierto, H. J. Gogas, A. Arance, Y.K. T. Flaherty, Overall survival in patients with BRAF-mutant melanoma receiving encorafenib plus binimetinib versus vemurafenib or encorafenib (COLUMBUS): a multicentre, open-label, randomised, phase 3 trial, The Lancet Oncology, pp. 1315-1327, 2018.
[9] Reinhard Dummer, Paolo A Ascierto, Helen J Gogas, Ana Arance, Mario Mandala, Gabriella Liszkay, Claus Garbe, Dirk Schadendorf, Ivana Krajsova, Ralf Gutzmer, Vanna Chiarion-Sileni, Caroline Dutriaux, Jan Willem B de Groot, Naoya Yamazaki, Carmen Loquai, Laure A Moutouh-de Parseval, Michael D Pickard, Victor Sandor,

Caroline Robert, Keith T Flaherty, Encorafenib plus binimetinib versus vemurafenib or encorafenib in patients with BRAF -mutant melanoma (COLUMBUS): a multicentre, open-label, randomised phase 3 trial, The Lancet Oncology 19 (5) (2018) 603–615, https://doi.org/10.1016/S1470-2045(18)30142-6.
[10] A.A. Samatar, Y.P.I. Poulikakos, Targeting RAS–ERK signalling in, Nature Reviews Drug Discovery (2014) 928–942.
[11] X. Wang, Y.K. Schleicher, Conformation-specific Inhibitors of Raf Kinases, Enzymes, pp. 41-66, 2013.
[12] H. Lavoie, Y.M. Therrien, Regulation of RAF Protein Kinases in ERK Signalling, Nat Rev Mol Cell Biol (2015) 281–298.
[13] Z. Karoulia, Y. Wu, T. A. Ahmed, Q. Xin, Y.P. I. Poulikakos, Integrated Model of RAF Inhibitor Action Predicts Inhibitor Activity against Oncogenic BRAF Signaling, Cancer Cell, p. 485–498, 2017.
[14] S.-H. Chen, Y. Zhang, R. D. Van Horn, T. Yin, Y.S.-B. Peng, That Function as Homodimers and Are Sensitive to Inhibition by RAF Dimer Inhibitor LY3009120, Cancer Discovery, p. 300 − 315, 2016.
[15] Hugo Lavoie, Neroshan Thevakumaran, Gwenaëlle Gavory, John J Li, Abbas Padeganeh, Sébastien Guiral, Jean Duchaine, Daniel Y L Mao, Michel Bouvier, Frank Sicheri, Marc Therrien, Inhibitors that stabilize a closed RAF kinase domain conformation induce dimerization, Nat Chem Biol 9 (7) (2013) 428–436, https://doi.org/10.1038/nchembio.1257.
[16] B. Agianian, Y.E. Gavathiotis, Current Insights of BRAF Inhibitors in Cancer, J. Med. Chem. (2018) 5775–5793.
[17] Sonja J. Heidorn, Carla Milagre, Steven Whittaker, Arnaud Nourry, Ion Niculescu-Duvas, Nathalie Dhomen, Jahan Hussain, Jorge S. Reis-Filho, Caroline J. Springer, Catrin Pritchard, Richard Marais, Kinase-Dead BRAF and Oncogenic RAS Cooperate to Drive Tumor Progression through CRAF, Cell 140 (2) (2010) 209–221, https://doi.org/10.1016/j.cell.2009.12.040.
[18] Poulikos I. Poulikakos, Chao Zhang, Gideon Bollag, Kevan M. Shokat, Neal Rosen, RAF inhibitors transactivate RAF dimers and ERK signalling in cells with wild-type BRAF, Nature 464 (7287) (2010) 427–430, https://doi.org/10.1038/nature08902.
[19] Georgia Hatzivassiliou, Kyung Song, Ivana Yen, Barbara J. Brandhuber, Daniel J. Anderson, Ryan Alvarado, Mary J.C. Ludlam, David Stokoe, Susan L. Gloor, Guy Vigers, Tony Morales, Ignacio Aliagas, Bonnie Liu, Steve Sideris, Klaus P. Hoeflich, Bijay S. Jaiswal, Somasekar Seshagiri, Hartmut Koeppen, Marcia Belvin, Lori S. Friedman, Shiva Malek, RAF inhibitors prime wild-type RAF to activate the MAPK pathway and enhance growth, Nature 464 (7287) (2010) 431–435, https://doi.org/10.1038/nature08833.
[20] M. Holderfield, M.M. Deuker, F. McCormick, Y.M. McMahon, Targeting RAF kinases for cancer therapy: BRAF-mutated melanoma and beyond, Nat. Rev. Cancer (2014) 455–467.
[21] N. Cope, C. Candelora, K. Wong, S. Kumar, Y.Z. Wang, Mechanism of BRAF Activation Through Biochemical Characterization of the Recombinant Full-Length Protein, Chembiochem , pp. 1988-1997, 2018.
[22] Zoi Karoulia, Yang Wu, Tamer A. Ahmed, Qisheng Xin, Julien Bollard, Clemens Krepler, Xuewei Wu, Chao Zhang, Gideon Bollag, Meenhard Herlyn, James A. Fagin, Amaia Lujambio, Evripidis Gavathiotis, Poulikos I. Poulikakos, An Integrated Model of RAF Inhibitor Action Predicts Inhibitor Activity against Oncogenic BRAF Signaling, Cancer Cell 30 (3) (2016) 501–503, https://doi.org/10.1016/j.ccell.2016.08.008.
[23] C. Zhang, W. Spevak, Y. Zhang, E.A. Burton, Y.G. Bollag, RAF inhibitors that evade paradoxical MAPK pathway activation, Nature 526 (2015) 583–586.
[24] C.H. Adelmann, G. Ching, L. Du, R.C. Saporito, Y.K.Y. Tsai, Comparative profiles of BRAF inhibitors: the paradox index as a predictor of clinical toxicity, Oncotarget 7 (21) (2016) 30453–30460.
[25] L.E. Campos, F.M. Garibotto, E. Angelina, J. Kos, Y.R.D. Enriz, Searching New Structural Scaffolds for BRAF Inhibitors. An Integrative Study using theoretical and experimental techniques, Bioorganic Chemistry (2019).
[26] M. Vettorazzi, E. Angelina, S. Lima, T. Gonec, Y.R.D. Enriz, An integrative study to identify novel scaffolds for sphingosine kinase 1 inhibitors, *Europ*, J Med. Chem. (2017) 461–481.
[27] P. Marvanova, T. Padrtova, T. Pekarek, J. Brus, Y.J. Jampilek, Synthesis and characterization of new 3-(4-arylpiperazin-1-yl)-2-hydroxypropyl 4-propoxybenzoates and their hydrochloride salts, Molecules, pp. 4-7, 2016a.
[28] P. Marvanova, T. Padrtova, K. Odehnalova, O. Hosik, Y.P. Mokry, Synthesis and determination of physicochemical properties of new 3-(4-arylpiperazin-1-yl)-2-hydroxypropyl 4-alkoxyethoxy-benzoates., Molecules, pp. 1682-1688, 2016b.
[29] T. Gonec, J. Kos, E. Nevin, R. Govender, Y.J. Jampilek, Preparation and biological properties of ring-substituted naphthalene-1-carboxanilides., Molecules, p. 9–11, 2014.
[30] T. Gonec, J. Kos, I. Zadrazilova, M. Pesko, Y.J. Jampilek, Antibacterial and herbicidal activity of ring-substituted 2-hydroxynaphthalene-1-carboxanilides, Molecules, pp. 9397-9419, 2013.
[31] T. Gonec, J. Kos, M. Pesko, J. Dohanosova, Y.J. Jampilek, Halogenated 1-hydroxynaphthalene-2-carboxanilides affecting photosynthetic electron transport in photosystem II, Molecules, pp. 15-17, 2017.
[32] J. Kos, I. Zadrazilova, M. Pesko, S. Keltosova, Y.J. Jampilek, Antibacterial and herbicidal activity of ring-substituted 3-hydroxynaphthalene-2-carboxanilides, Molecules, pp. 7977-7997, 2013.
[33] J. Kos, E. Nevin, M. Soral, I. Kushkevych, Y.J. Jampilek, Synthesis and anti-mycobacterial properties of ring-substituted 6-hydroxynaphthalene- 2-carboxanilides, Bioorg. Med. Chem. (2015) 20–25.
[34] G.M. Morris, R. Huey, W. Lindstrom, M.F. Sanner, Y.A.J. Olson, AutoDock4 and AutoDockTools4: automated docking with selective receptor flexibility, J. Comput. Chem. (2009) 2785–2791.
[35] AMBER 2014, 2014.
[36] K. Lindorff-Larsen, S. Piana, K. Palmo, P. Maragakis, Y.D. E. Shaw, Improved Side-Chain Torsion Potentials for the Amber ff99SB Protein Force Field, Proteins, p. 1950–1958, 2010.
[37] J. Wang, R.M. Wolf, J.W. Caldwell, P.A. Kollman, Y.D.A. Case, Development and Testing of a General Amber Force Field, J. Comput. Chem. (2004) 1157–1174.
[38] A.D. Becke, Density-functional Thermochemistry. III. The Role of Exact Exchange, J. Chem. Phys. (1993) 5648–5652.
[39] U. Essmann, L. Perera, Y.M.L. Berkowitz, Smooth Particle Mesh Ewald Method, J. Chem. Phys. (1995).
[40] D. R. Roe, Y.T. E. Cheatham, PTRAJ and CPPTRAJ: Software for Processing and Analysis of Molecular Dynamics Trajectory Data, J. Chem. Theory Comput., p. 3084–3095, 2013.
[41] S. Genheden, Y.U. Ryde, The MM/PBSA and MM/GBSA Methods to Estimate Ligand-Binding Affinities, Expert Opin. Drug Discov. (2015) 449–461.
[42] U. Koch, Y.P.L. Popelier, Characterization of C-H-O Hydrogen Bonds on the Basis of the Charge Density, J. Phys. Chem. (1995) 9747–9754.
[43] C.F. Matta, N. Castillo, Y.R.J. Boyd, Extended Weak Bonding Interactions in DNA: π-Stacking (Base − Base), Base − Backbone, and Backbone − Backbone Interactions, J. Phys. Chem. (2005) 563–578.
[44] R. A. Mosquera, M. J. Moa, L. Estevez, M. Mandado, Y.A. M. Graña, An Electron Density-Based Approach to the Origin of Stacking Interactions, de Quantum Biochemistry, Weinheim, Germany, Ed. WILEY-VCH Verlag GmbH & Co, 2010, pp. 365-387.
[45] R.F.W. Bader, Atoms in molecules, Acc. Chem. Res. (1985) 9–15.
[46] R.F. Bader, A quantum theory of molecular structure and its applications, Chem. Rev. (1991) 893–928.
[47] R. F. Bader, The Quantum Mechanical Basis of Conceptual Chemistry, Monatshefte für Chemie, p. 819–854, 2005.
[48] R.F. Bader, Atoms in Molecules, *Encycl*, Comput. Chem. (1998).
[49] S.A. Andujar, R.D. Tosso, F.D. Suvire, E. Angelina, Y.R.D. Enriz, Searching the "Biologically Relevant"Conformation of Dopamine: A Computational Approach, J. Chem. Inf. Model. (2012) 99–112.
[50] R.D. Tosso, S.A. Andujar, L. Gutierrez, E. Angelina, Y.R.D. Enriz, Molecular Modeling Study of Dihydrofolate Reductase Inhibitors. Molecular Dynamics Simulations, Quantum Mechanical Calculations, and Experimental Corroboration, J. Chem. Inf. Model. (2013) 2018–2032.
[51] F. Chen, Multiwfn: A multifunctional wavefunction analyzer, J. Comput., pp. 580-592, 2012.
[52] T. A. Keith, T. G. S. AIMAll (Version 19.02.13), Overl. Park KS, USA, 2019.
[53] M. J. Frisch, G. W. Trucks, H. B. Schlegel, G. E. Scuseria, Y.D. J. Fox, Gaussian 16, Revision B.01. 2016, Wallingford CT, 2016.
[54] C. Lee, W. Yang, Y.R.G. Parr, Development of the Colle-Salvetti Correlation-Energy Formula into a Functional of the Electron Density, Phys. Rev. B. Condens. Matter (1988) 785–789.
[55] W.J. Hehre, R. Ditchfield, Y.J.A. Pople, Self—Consistent Molecular Orbital Methods. XII. Further Extensions of Gaussian—Type Basis Sets for Use in Molecular Orbital Studies of Organic Molecules, J. Chem. Phys. (1972).
[56] S. Grimme, Semiempirical GGA-Type Density Functional Constructed with a Long-Range Dispersion Correction, J. Comput. Chem. (2006) 1787–1799.